

Data-driven Augmentation of Turbulence Model in Three-dimensional Flows Via Sequential Correction

Chenyu Wu[†], Shaoguang Zhang[‡], Yufei Zhang^{*, ††, §}

School of Aerospace Engineering, Tsinghua University

Abstract

Classic turbulence models often struggle to accurately predict complex flows that involve phenomena such as flow separation. Although data-driven techniques have emerged to address these shortcomings by augmenting classical models with correction terms, most existing research has concentrated on two-dimensional (2D) cases. Therefore, the performance of these corrected models in complex three-dimensional (3D) flows remains an underexplored area. This study addresses this gap by enhancing a data-driven turbulence model, the SST-CND (shear stress transport-conditioned) model, which was originally trained on 2D separated flows. An additional correction term, β_{3D} , is introduced to account for 3D effects. The distribution of this term is initially determined through a 3D field inversion process using high-fidelity data obtained from the flow around a cube. An explicit algebraic expression for β_{3D} is then derived through symbolic regression and formulated to degrade to zero in 2D cases. This new expression is integrated into the original model, resulting in the SST-CND3D model. The performance of the SST-CND3D model is evaluated across a range of flows. In 2D flows, including the separated flow around a hump, flow over a flat plate, and flow around a multi-element airfoil, the SST-CND3D model performs identically to its 2D-trained predecessor. However, the model exhibits superior performance in 3D flows, such as the flow around a cube and the complex, real-world JAXA standard model high-lift configuration. These findings indicate that a sequential correction approach, constructing a 3D correction term that vanishes in 2D on top of a 2D-trained model, constitutes a promising method for developing data-driven turbulence models that perform accurately in 3D while preserving their effectiveness in 2D.

Keywords: Turbulence modeling; Three-dimensional flows; Field inversion; High-lift configuration

[†] Ph.D. student, School of Aerospace Engineering, Tsinghua University

[‡] Post-doc researcher, School of Aerospace Engineering, Tsinghua University

^{*} Associate professor, AIAA associate fellow, School of Aerospace Engineering, Tsinghua University (Corresponding author:

zhangyufei@tsinghua.edu.cn)

^{††} Associate professor, State Key Laboratory of Advanced Space Propulsion, Tsinghua University, 100084, Beijing

[§] Associate professor, Caofeidian Laboratory, 063200, Tangshan, China

1. Introduction

Turbulence occurs in numerous engineering applications and can significantly affect the performance of engineering designs, making the analysis of turbulence highly important. In computational fluid dynamics (CFD), researchers often employ turbulence simulation methods to analyze turbulent flows. Among these methods, the Reynolds-averaged Navier-Stokes (RANS) equations are widely used in real-world engineering applications due to their high efficiency and low computational cost. However, evidence has shown that traditional RANS turbulence models often fail in complex flow conditions, such as flows involving separation [1][2][3] and flows around high-lift devices [4][5]. Duraisamy et al. [6] predicted that the RANS method will continue to serve as the workhorse of CFD in the future due to the immature state of scale-resolving methods. Therefore, considering the broad applicability of the RANS method, it is essential to enhance the accuracy of RANS turbulence models in complex flows.

Recently, researchers have increasingly used data-driven techniques to improve the ability of RANS turbulence models to predict complex separated flows [7]. Several studies have focused on improving the expression of Reynolds stress. Julia et al. [8] proposed a tensor-basis neural network to predict the nonlinear Reynolds stress, enhancing the model's accuracy in separated flows. Yin et al. [9] developed a novel feature decomposition method to increase the smoothness of the Reynolds stress predicted by the neural network. Tang et al. [10] and Zhao et al. [11] applied symbolic learning methods to construct analytical expressions for nonlinear Reynolds stress based on high-fidelity data. Another group of studies has focused on correcting the transport equations of turbulence models. Singh et al. [12] introduced the field inversion and machine learning (FIML) method to quantify functional errors in the transport equations caused by assumptions made by modelers using high-fidelity data. Holland et al. [13] developed a variant of the FIML method that trains the neural network directly using the gradient produced by field inversion, achieving physics-consistent training. Wu et al. [14] employed a symbolic regression method to train an analytical expression for the correction term based on field inversion data, resulting in a more interpretable FIML model with strong generalizability. Zhang et al. [15] applied the data-driven SST-CND (shear-stress-transport-conditioned) model trained by Wu et al. [16] using FIML to three-dimensional complex high-lift configurations. The results demonstrated that the SST-CND model performed better than the SST

model but still showed some deviation from experimental data. Zhang et al. attributed this discrepancy to the lack of three-dimensional (3D) data in the training set of the SST-CND model, which was trained only on two-dimensional (2D) cases.

Most studies on data-driven turbulence models train models using 2D high-fidelity data, with only a few utilizing 3D data. Ho et al. [17] performed FIML on a mixed dataset that included field inversion data from a 3D hill. The machine learning model developed by Ho et al. was tested on a 3D non-axisymmetric bump, yielding favorable results. Yan et al. [18] conducted FIML on the axisymmetric 3D FAITH hill [19], analyzing the effect of the number of samples used in machine learning on the accuracy of the trained neural network. Sun et al. [20] trained a data-driven turbulence model based on neural networks using 3D wing data at high Reynolds numbers. The model was deployed on a heterogeneous supercomputing environment, demonstrating both high accuracy and efficiency. Steiner et al. [21] focused on 3D wind farms and derived analytical correction terms for the RANS equations using large eddy simulation data through symbolic regression. In all the studies mentioned above, 3D data were employed to develop data-driven turbulence models. However, all correction terms were derived from scratch without considering their impact on 2D flows, which can compromise the baseline model’s accuracy in 2D flows and limit the model’s generalizability.

This study proposes a sequential correction approach to enhance the performance of the SST-CND model in three-dimensional (3D) complex flows using 3D data. The method involves constructing an additional correction term, β_{3D} , directly on top of the SST-CND model’s original correction term (β_{CND}). The distribution of β_{3D} is first obtained through field inversion of the flow around a cube. Symbolic regression is then employed to construct an explicit expression passing through the origin for β_{3D} as a function of local flow features that are non-zero only in 3D flows. This deliberate design ensures that the β_{3D} correction is inactive in two-dimensional (2D) cases, which is crucial because the original SST-CND model already performs well in these scenarios, and maintaining that performance is essential. The resulting SST-CND3D model exhibits identical performance to its predecessor on various 2D test cases while demonstrating superior accuracy in 3D complex high-lift configurations, such as the JAXA standard model. This study indicates that constructing a 3D correction term on top of a model trained exclusively on 2D data is a logical and effective approach to enhancing a model’s 3D performance without compromising its baseline

accuracy in 2D flows.

2. Methods

In this section, the model on which the 3D correction term is developed, namely the SST-CND model, is first introduced. Then, the field inversion method and the symbolic regression method utilized to construct the β_{3D} correction term are briefly discussed.

2.1. Formulation of the SST-CND model and the β_{3D} correction term

This study aims to enhance the performance of the SST-CND [16] model in 3D complex flows. The SST-CND model is a data-driven turbulence model trained using conditioned field inversion and symbolic regression. It performs effectively in predicting a series of 2D complex separated flows, including the NASA hump and NLR-7301 multi-element airfoil. It also maintains the original SST (shear-stress-transport) model's accuracy in simple wall-attached flows, such as the zero-pressure-gradient turbulent flat plate. The formulation of the SST-CND model is presented below (for incompressible flow with constant density).

$$\begin{aligned}\frac{Dk}{Dt} &= P_k - \beta^* k \omega + \nabla \cdot [(v + \sigma_k v_T) \nabla k] \\ \frac{D\omega}{Dt} &= \frac{\gamma}{v_T} P_k - \beta \theta \omega^2 + \nabla \cdot [(v + \sigma_\omega v_T) \nabla \omega] + \frac{2(1 - F_1) \sigma_\omega^2}{\omega} \nabla k \cdot \nabla \omega\end{aligned}\quad (1)$$

k is the turbulence kinetic energy; ω is the specific dissipation rate; β^* is a constant and equals 0.09; P_k is the production of k and is defined as follows:

$$\begin{aligned}P_k &= \min\left(\tau_{ij} \frac{\partial u_i}{\partial x_j}, 10\beta^* k \omega\right) \\ \tau_{ij} &= 2v_T S_{ij} - \frac{2}{3} k \delta_{ij} \\ S_{ij} &= \frac{1}{2} \left(\frac{\partial u_i}{\partial x_j} + \frac{\partial u_j}{\partial x_i}\right)\end{aligned}\quad (2)$$

τ_{ij} is called the Reynolds stress; v_T is the eddy viscosity and is defined as follows:

$$v_T = \frac{a_1 k}{\max(a_1 \omega, SF_2)}\quad (3)$$

a_1 is a constant equal to 0.31. β in Eq. (1) (appearing as a multiplier in front of the destruction

term of the ω equation) is the correction term derived through conditioned field inversion and symbolic regression. The training data are entirely 2D, including the NASA hump case [22] and the curved backward-facing step case [23]. For details of the training process, please refer to Ref [16].

The formulation of β is provided as follows:

$$\begin{aligned}
\beta &= \beta_{CND} f_d + 1 \\
\beta_{CND} &= \min(0.00435\lambda_2^2, 3.80686) \\
\lambda_2 &= \text{tr} \left[\left(\frac{\mathbf{\Omega}}{\beta^* \omega} \right)^2 \right], \Omega_{ij} = \frac{1}{2} \left(\frac{\partial u_i}{\partial x_j} - \frac{\partial u_j}{\partial x_i} \right) \\
f_d &= 1 - \tanh[(8r_d)^3], r_d = \frac{v + v_T}{\kappa^2 d^2 \sqrt{\frac{\partial u_i}{\partial x_j} \frac{\partial u_i}{\partial x_j}}}
\end{aligned} \tag{4}$$

Note that if $\beta = 1$, the model degrades to the baseline SST model. The definitions of the functions in Eqs. (1) and (3) are listed below:

$$\begin{aligned}
F_1 &= \tanh(\xi_1^4), \xi_1 = \min \left[\max \left(\frac{\sqrt{k}}{\beta^* \omega d}, \frac{500\nu}{d^2 \omega} \right), \frac{4\sigma_{\omega 2} k}{CD_{k\omega} d^2} \right] \\
CD_{k\omega} &= \max \left(\frac{2\sigma_{\omega 2}}{\omega} \nabla k \cdot \nabla \omega, 10^{-10} \right) \\
F_2 &= \tanh(\xi_2^2), \xi_2 = \max \left(\frac{2\sqrt{k}}{\beta^* \omega d}, \frac{500\nu}{d^2 \omega} \right), S = \sqrt{2S_{ij}S_{ij}}
\end{aligned} \tag{5}$$

d is the distance to the closest wall; $\sigma_{\omega 2}$ is a constant. Other parameters are defined using the blending function F_1 :

$$\begin{aligned}
\gamma &= F_1 \gamma_1 + (1 - F_1) \gamma_2, \theta = F_1 \theta_1 + (1 - F_1) \theta_2 \\
\sigma_k &= F_1 \sigma_{k1} + (1 - F_1) \sigma_{k2}, \sigma_\omega = F_1 \sigma_{\omega 1} + (1 - F_1) \sigma_{\omega 2}
\end{aligned} \tag{6}$$

The parameters in Eq. (6) (γ_1 and γ_2) are all constants. The values can be found in Ref [24].

The SST-CND model was successfully applied to 3D complex high-lift configurations [15] such as the JAXA Standard Model (JSM). The SST-CND model demonstrates better accuracy compared to the baseline SST model. However, the maximum lift coefficient (C_L) and the stall angle of attack (AOA) are still underpredicted by the SST-CND model. Zhang et al. [15] attributed this inaccuracy to the SST-CND model's lack of 3D training data and its inability to capture 3D effects. Therefore, adding 3D data to the training set can potentially improve the model's performance in complex 3D flows such as the JSM. However, retraining the model from scratch using a mixed dataset of 2D and 3D data is undesirable. The SST-CND model already performs well in a series of 2D separated flows, and retraining can compromise this established performance. Hence, a method

is required to incorporate 3D training data non-intrusively, enhancing 3D performance while preserving the model's existing 2D accuracy.

This study addresses the aforementioned issue by introducing an additional correction term β_{3D} , into the SST-CND model and formulating an expression for β_{3D} through a sequential learning approach:

$$\beta = (\beta_{CND} + \beta_{3D})f_a + 1 \quad (7)$$

The spatial distribution of β_{3D} is determined through field inversion of the flow around a cube (3D). Then, symbolic regression is applied to construct an expression for β_{3D} that vanishes in 2D flows. In this manner, the 3D training data are injected exclusively into the β_{3D} term, avoiding retraining of the β_{CND} term. A β_{3D} term that reduces to zero in 2D scenarios also ensures that the model's performance in 2D flows remains unaffected.

2.2. Field inversion

In this section, the field inversion method utilized to obtain the spatial distribution of β_{3D} is introduced. During the field inversion process, the distribution of β_{3D} is adjusted by an optimization algorithm to match the RANS-predicted velocity with the high-fidelity data (i.e., experimental data). The β_{3D} distribution that minimizes the discrepancy between the RANS-predicted velocity and the high-fidelity data is defined as the optimal β_{3D} distribution. In this study, it is obtained by solving the following specific optimization problem.

$$\min_{\beta_{3D}} J = \lambda_{obs} \sum_i [u_i^{exp} - u_i(\beta_{3D})]^2 + \lambda_{prior} \sum_j \beta_{3D,j}^2 \quad (8)$$

$\beta_{3D,j}$ is the value of β_{3D} in the j^{th} cell of the computational mesh; β_{3D} is the vector whose j^{th} element is $\beta_{3D,j}$; u_i^{exp} is the i^{th} high-fidelity data point of streamwise velocity provided by the experiment; $u_i(\beta_{3D})$ is the RANS-predicted streamwise velocity corresponding to the i^{th} high-fidelity data point given the vector β_{3D} . The optimal distribution of β_{3D} corresponds to the optimal β_{3D} vector that can minimize J in Eq. (8). λ_{obs} and λ_{prior} are two constants utilized to scale the two terms in Eq. (8). The first term in Eq. (8) measures the discrepancy between the RANS-predicted streamwise velocity and the high-fidelity data provided by the experiment. The second term in Eq. (8) measures the deviation of β_{3D} from its default value, namely, zero.

A gradient-based optimization program, SNOPT [25], is employed to solve the optimization

problem in Eq. (8). The discrete adjoint method [26] is utilized to compute the gradient of the objective function in Eq. (8) with respect to $\boldsymbol{\beta}_{3D}$. The algorithm of the discrete adjoint method is briefly introduced. In CFD simulations, the objective function J in Eq. (8) and the residual of the equations \mathbf{R} can be treated as functions of the flow variable \mathbf{w} (including velocity, pressure, and turbulent variables) and the correction term $\boldsymbol{\beta}_{3D}$:

$$J(\mathbf{w}, \boldsymbol{\beta}_{3D}), \mathbf{R}(\mathbf{w}, \boldsymbol{\beta}_{3D}) \quad (9)$$

The output of \mathbf{R} is a vector. Suppose the simulation is executed on a mesh with N cells; then, the output of \mathbf{R} is mN , where m is the number of governing equations. The dimension of \mathbf{w} is the same as that of \mathbf{R} since the number of flow variables in each cell equals the number of governing equations. For a converged solution (where the output of the residual function is zero), \mathbf{w} is also a function of $\boldsymbol{\beta}_{3D}$ defined by the following implicit relationship.

$$\mathbf{R}(\mathbf{w}(\boldsymbol{\beta}_{3D}), \boldsymbol{\beta}_{3D}) = 0 \quad (10)$$

For every $\boldsymbol{\beta}_{3D}$, the corresponding converged RANS solution $\mathbf{w}(\boldsymbol{\beta}_{3D})$ should satisfy the relationship above. J can be treated as a function of $\boldsymbol{\beta}_{3D}$ using the implicit relationship between \mathbf{w} and $\boldsymbol{\beta}_{3D}$ ($\mathbf{w}(\boldsymbol{\beta}_{3D})$):

$$J(\mathbf{w}(\boldsymbol{\beta}_{3D}), \boldsymbol{\beta}_{3D}) \quad (11)$$

Then, the gradient of J with respect to $\boldsymbol{\beta}_{3D}$ can be written as follows:

$$\nabla J = \frac{\partial J}{\partial \mathbf{w}} \frac{d\mathbf{w}}{d\boldsymbol{\beta}_{3D}} + \frac{\partial J}{\partial \boldsymbol{\beta}_{3D}} \quad (12)$$

The Jacobians $(\frac{\partial J}{\partial \mathbf{w}}, \frac{\partial J}{\partial \boldsymbol{\beta}_{3D}})$ can be computed by automatic differentiation. However, $\frac{d\mathbf{w}}{d\boldsymbol{\beta}_{3D}}$ is hard to compute because \mathbf{w} is obtained by CFD iterations, not by a single function evaluation. The discrete adjoint method uses the relationship in Eq. (10) to calculate $\frac{d\mathbf{w}}{d\boldsymbol{\beta}_{3D}}$. Differentiating Eq. (10) with respect to $\boldsymbol{\beta}_{3D}$, yields:

$$\frac{\partial \mathbf{R}}{\partial \mathbf{w}} \frac{d\mathbf{w}}{d\boldsymbol{\beta}_{3D}} + \frac{\partial \mathbf{R}}{\partial \boldsymbol{\beta}_{3D}} = 0 \quad (13)$$

$\frac{\partial \mathbf{R}}{\partial \mathbf{w}}$ and $\frac{\partial \mathbf{R}}{\partial \boldsymbol{\beta}_{3D}}$ are Jacobians and can be evaluated by automatic differentiation, since \mathbf{R} can be computed by a single function call. Then, $\frac{d\mathbf{w}}{d\boldsymbol{\beta}_{3D}}$ can be calculated by:

$$\frac{d\mathbf{w}}{d\boldsymbol{\beta}_{3D}} = - \left(\frac{\partial \mathbf{R}}{\partial \mathbf{w}} \right)^{-1} \frac{\partial \mathbf{R}}{\partial \boldsymbol{\beta}_{3D}} \quad (14)$$

Therefore, Eq. (12) can be described as follows:

$$\nabla J = \frac{\partial J}{\partial \boldsymbol{\beta}_{3D}} - \frac{\partial J}{\partial \mathbf{w}} \left(\frac{\partial \mathbf{R}}{\partial \mathbf{w}} \right)^{-1} \frac{\partial \mathbf{R}}{\partial \boldsymbol{\beta}_{3D}} \quad (15)$$

Now, the adjoint variable $\boldsymbol{\psi}$ is defined as follows:

$$\boldsymbol{\psi}^T = - \frac{\partial J}{\partial \mathbf{w}} \left(\frac{\partial \mathbf{R}}{\partial \mathbf{w}} \right)^{-1} \quad (16)$$

Then, the gradient of J is simply:

$$\nabla J = \frac{\partial J}{\partial \boldsymbol{\beta}_{3D}} + \boldsymbol{\psi}^T \frac{\partial \mathbf{R}}{\partial \boldsymbol{\beta}_{3D}} \quad (17)$$

The definition in Eq. (16) can be expressed as follows:

$$\boldsymbol{\psi} = - \left[\left(\frac{\partial \mathbf{R}}{\partial \mathbf{w}} \right)^T \right]^{-1} \left(\frac{\partial J}{\partial \mathbf{w}} \right)^T \quad (18)$$

That is to say, $\boldsymbol{\psi}$ can be obtained by solving the following linear system:

$$\left(\frac{\partial \mathbf{R}}{\partial \mathbf{w}} \right)^T \boldsymbol{\psi} = - \left(\frac{\partial J}{\partial \mathbf{w}} \right)^T \quad (19)$$

Based on the analysis given above, the execution steps of the discrete adjoint method can be summarized as follows:

- (1) Given the $\boldsymbol{\beta}_{3D}$ distribution $\boldsymbol{\beta}_{3D}$, solve the RANS equations until convergence (until $\mathbf{R}(\mathbf{w}(\boldsymbol{\beta}_{3D}), \boldsymbol{\beta}_{3D}) = 0$ is fulfilled), obtaining $\mathbf{w}(\boldsymbol{\beta}_{3D})$.
- (2) Evaluate the objective function J and the residual function \mathbf{R} , and obtain the Jacobians $\left(\frac{\partial \mathbf{R}}{\partial \mathbf{w}}, \frac{\partial \mathbf{R}}{\partial \boldsymbol{\beta}_{3D}}, \frac{\partial J}{\partial \mathbf{w}}, \text{ and } \frac{\partial J}{\partial \boldsymbol{\beta}_{3D}} \right)$ during this process using automatic differentiation.
- (3) Solve the linear system in Eq. (19) to obtain the adjoint variable $\boldsymbol{\psi}$.
- (4) Compute the gradient of J with respect to $\boldsymbol{\beta}_{3D}$ based on Eq. (17).

In this study, the open-source package DAfoam [27][28] is utilized to solve the RANS problem and the discrete adjoint problem. The automatic differentiation in DAfoam is supported by the open-source package CODIPACK [29].

2.3. Symbolic regression

In this part, the symbolic regression (SR) method utilized to construct the analytical expression of $\boldsymbol{\beta}_{3D}$ is briefly introduced. The learning target of SR is the optimal distribution of $\boldsymbol{\beta}_{3D}$ obtained through the field inversion process. As mentioned earlier, the expression of $\boldsymbol{\beta}_{3D}$ should vanish in 2D flows. This requirement necessitates a careful selection of the input features used in symbolic

regression. For 2D incompressible flows, the third and fourth invariants of the Reynolds stress are identically zero [30]. The proof of $\lambda_3 = 0$ and $\lambda_4 = 0$ is provided in the appendix. This characteristic can be exploited to construct a series of features that are zero in 2D flows. The features constructed through the transformation of λ_3, λ_4 , as well as those obtained by multiplying λ_3, λ_4 with other features, are listed in Table 1. All of these features are zero in 2D incompressible flows, enabling them to distinguish between 2D and 3D flows, allowing β_{3D} to vanish in 2D cases. Some features were used in classical turbulence modeling, such as $|\lambda_4|$, which appears in the Wilcox $k - \omega$ 2006 model [31]. In contrast, other features are constructed artificially.

Table 1. Input features of symbolic regression.

Name	Definition	Physical Meaning
λ_3	$\text{tr}(\widehat{\mathcal{S}}^3)$	The third and fourth independent invariants of tensors $\widehat{\mathcal{S}}$ and $\widehat{\mathcal{Q}}$, where $\widehat{\mathcal{S}} = \frac{k}{\varepsilon} \mathcal{S}, \widehat{\mathcal{Q}} = \frac{k}{\varepsilon} \mathcal{Q}, \varepsilon = \beta^* k \omega$. \mathcal{S} and \mathcal{Q} are the strain rate tensor and the rotation rate tensor. The invariants λ_3 and λ_4 are related to the strength and the structure of the vorticity in the flow field. They are theoretically zero in 2D incompressible flows.
λ_4	$\text{tr}(\widehat{\mathcal{Q}}^2 \widehat{\mathcal{S}})$	
l_{14}	$\lambda_1 \lambda_4, \lambda_1 = \text{tr}(\widehat{\mathcal{S}}^2)$	λ_1 is utilized to measure the strength of the strain rate in the flow.
l_{13}	$\lambda_1 \lambda_3, \lambda_1 = \text{tr}(\widehat{\mathcal{S}}^2)$	Multiplying λ_1 with λ_4 or λ_3 makes the feature zero in 2D flows.
$ \lambda_3 $	$ \text{tr}(\widehat{\mathcal{S}}^3) $	The magnitude of λ_3 and λ_4 . It is a simple transformation of the features. Note that $ \lambda_4 $ was used in the Wilcox $k - \omega$ turbulence model to distinguish the round jet [31].
$ \lambda_4 $	$ \text{tr}(\widehat{\mathcal{Q}}^2 \widehat{\mathcal{S}}) $	
$ \lambda_3 \text{Re}_\Omega$	$ \text{tr}(\widehat{\mathcal{S}}^3) \frac{ \mathcal{Q} d^2}{\nu}$	Re_Ω is originally utilized to distinguish the separated shear layer from the wall. These two features are constructed artificially to be related to separated shear layers and to be 0 in 2D incompressible flow at the same time.
$ \lambda_4 \text{Re}_\Omega$	$ \text{tr}(\widehat{\mathcal{Q}}^2 \widehat{\mathcal{S}}) \frac{ \mathcal{Q} d^2}{\nu}$	

In this study, the open-source SR software PySR [32] is employed to derive an analytical expression for β_{3D} . The element functions employed in the SR process are listed in Table 2. PySR selects the features in Table 1 and the functions in Table 2 to assemble the expression for β_{3D} . It utilizes an evolutionary algorithm with annealing to fit the expressions to the data. The L2 distance

loss function (the default in PySR) is adopted to evaluate the fitting quality.

$$loss(E) = \sum_j [\beta_{3D,j} - y_j]^2 \quad (20)$$

E Stands for an expression; y_j is the expression's prediction of the j^{th} data point; PySR also defines a metric $C(E)$ to measure the complexity of the expression E . This study determines $C(E)$ by:

$$C(E) = N_{opr.} + 4N_{const.} + 2N_{var.} \quad (21)$$

$N_{opr.}$ is the number of operators in E ; $N_{const.}$ is the number of constants; $N_{var.}$ is the number of variables. The maximum allowed $C(E)$ is set to 16. A higher weight is assigned to the variables to encourage PySR to perform feature selection, while an even higher weight is set for the constants to prevent PySR from overfitting by using too many constants. During the SR process, PySR maintains the best expressions across various complexity levels, allowing the user to select the most suitable expression by balancing complexity and loss.

Table 2. List of element functions used in symbolic regression

Operator type	Operators
Binary operators	$(\cdot) + (\cdot), (\cdot) - (\cdot), (\cdot) \times (\cdot), (\cdot) \div (\cdot), (\cdot)^{(\cdot)}, \min(\cdot, \cdot), \max(\cdot, \cdot)$
Unary operators	$\exp(\cdot), \tanh(\cdot), \frac{1}{1 + (\cdot)}, \frac{1}{(\cdot)}$

3. Model training

This section discusses the model training process, specifically the construction of the β_{3D} term. First, field inversion is conducted on the flow around a cube to determine the optimal β_{3D} distribution. Then, SR is applied to formulate the analytical expression of β_{3D} . The final model, which integrates the constructed β_{3D} expression, is referred to as the SST-CND3D model.

3.1. The field inversion of the flow around a cube

The flow around a cube is analyzed in this part. This case was investigated experimentally by Martinuzzi et al. [33]. The flow field exhibits symmetry; therefore, only half of the computational domain is considered. The computational mesh is shown in Figure 1(a). consisting of approximately half a million cells. The side view of the computational domain is presented in Figure 1(b). The

height of the cube is H , and the channel height is $2H$, which aligns with the experimental setup [33]. H is set to 1 m in this study. The computational domain is $4.5H$ wide and $14.5H$ long, with the cube positioned $3.5H$ downstream of the inlet. The origin of the coordinate system is located at the intersection of the frontal lower edge of the cube and the symmetry plane. The inlet velocity follows a well-developed channel flow profile, with a bulk velocity of 0.6 m/s . The Reynolds number, based on the bulk velocity and cube height, is set to 5×10^4 , consistent with the dataset provided in Ref. [33]. Figure 2 shows the high-fidelity data points (dark green dots) on the symmetry plane used in the field inversion process. These points correspond to the experimental velocity profiles at three positions ($x = 0.5 \text{ m}$, $x = 2.5 \text{ m}$, $x = 4.0 \text{ m}$) on the symmetry plane, as obtained by Martinuzzi et al. [33].

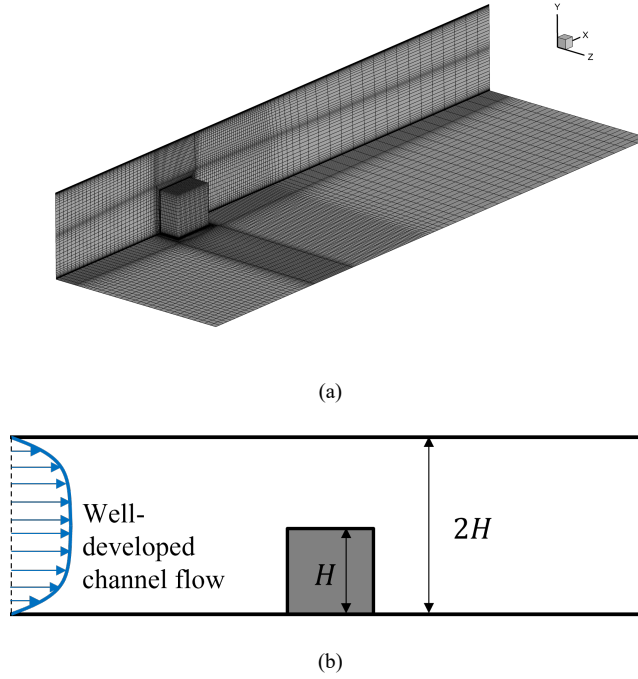


Figure 1. Computational domain of the cube case: (a) Computational mesh, (b) Side view of the domain

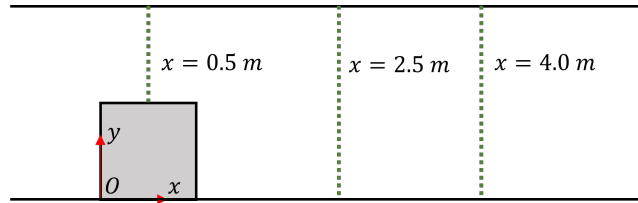


Figure 2. Location of the high-fidelity datapoints

The objective function used in the field inversion process is:

$$\min_{\beta_{3D}} J = 1.0 \sum_i [u_i^{exp} - u_i(\beta_{3D})]^2 + 1 \times 10^{-7} \sum_j \beta_{3D,j}^2 \quad (22)$$

The number of high-fidelity data points is approximately 100. The optimization of the field

inversion process runs for 225 steps (225 gradient evaluations), and the history is shown in Figure 3. The optimization approximately achieves convergence. Figure 4(a) indicates that the velocity profiles after the field inversion process match the high-fidelity data much better compared to the baseline SST-CND model (the model without β_{3D} augmentation but with the β_{CND} term). Figure 4(b) shows that the pressure distribution after the field inversion agrees better with the experiment [33]. The reference velocity for C_p is taken as the bulk velocity. The experimental data are adjusted to ensure $C_p = 0$ at the outlet, matching the CFD settings. The results of the baseline SST model (without any correction term) in Figure 4 are also plotted for reference. Figure 5(a) shows the contour of β_{3D} on the symmetry plane. β_{3D} is mainly activated in the separated shear layer starting from the frontal edge of the cube and the region immediately in front of the cube. Figure 5(b) and Figure 5(c) indicate that the β_{3D} correction term is also activated in the separated shear layer originating from the side edge of the cube.

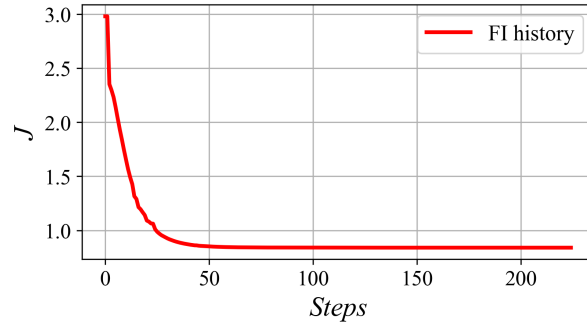


Figure 3. Convergence history of the objective function J

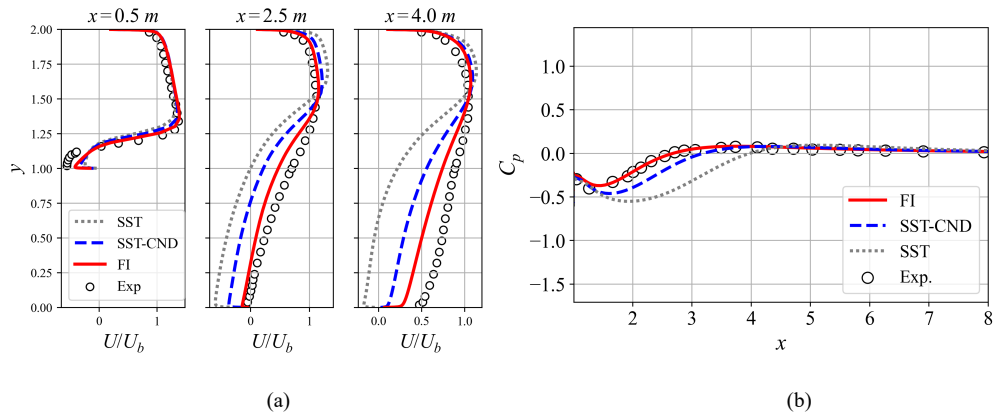


Figure 4. Flowfield after the field inversion, (a) Velocity profiles, (b) C_p distribution

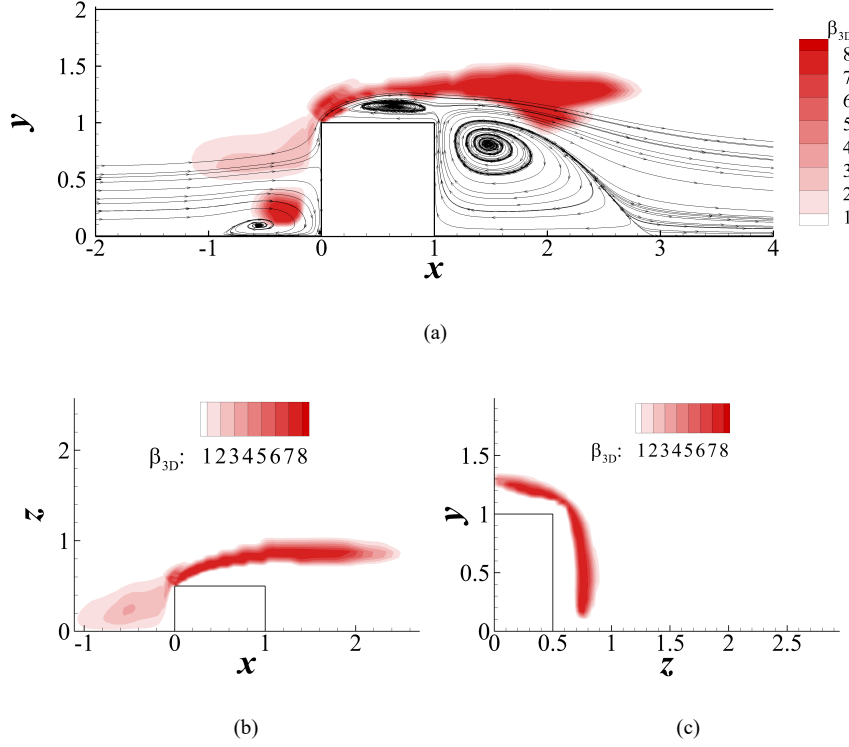


Figure 5. Contour of β_{3D} after field inversion, (a) on the symmetry plane ($z = 0$), (b) on the $y = 0.5$ m plane, (c) on the $x = 0.5$ m plane

3.2. Constructing the expression of the β_{3D} term

The expression of the β_{3D} term is constructed using symbolic regression based on the field inversion data. For the construction of the training dataset, all the cells in the bounding box ($x \times y \times z$): $[-1.5 \text{ m}, 5.5 \text{ m}] \times [0.2 \text{ m}, 1.8 \text{ m}] \times [0.0 \text{ m}, 1.5 \text{ m}]$ are first extracted. The total number of cells in this bounding box is approximately 1×10^5 , which is too large for symbolic regression. Therefore, random down-sampling is performed among these cells to select only 1×10^4 of them as the training dataset. Using the features listed in Table 1 and the element functions in Table 2, PySR obtained a series of expressions with varying complexities. The final expressions are shown in Table 3. The loss of the expressions against the complexity is also illustrated in Figure 6. The loss decreases only slightly when the complexity exceeds 12, while extra features and complex functional structures are introduced. It is also required that the expression yields zero output in 2D flows (when the input features are zero) to switch off the augmentation in 2D scenarios. Based on the complexity-loss relationship and this requirement, the expression with

a complexity of 12 is selected as the expression for β_{3D} :

$$\beta_{3D} = \min(0.38399717|\lambda_4|, 7.041212) \quad (23)$$

This produces $\beta_{3D} = 0$ in 2D flows since $|\lambda_4| = 0$ in such cases. Eq. (23) is then integrated into the incompressible solver SimpleFoam of OpenFOAM [34]. It is also implemented in the compressible solver CFL3D [35]. In CFL3D, when computing λ_4 , the correction proposed in Ref. [31] is utilized:

$$\lambda_4 = \text{tr}\left(\widehat{\Omega}^2(\widehat{\mathcal{S}} - q\mathbf{I})\right), q = 0.5\text{tr}(\widehat{\mathcal{S}}) \quad (24)$$

\mathbf{I} is the identical tensor. This correction ensures that λ_4 is also identically 0 in 2D compressible flows since $\widehat{\mathcal{S}} - q\mathbf{I}$ is traceless for any 2D scenarios. Note that this correction has no effect for incompressible flows because $q = 0$ in such flows. The model integrated with the β_{3D} term is named as the SST-CND3D model.

Table 3. The final expressions obtained by PySR

Complexity	Loss	Expression
2	35.63232	$ \lambda_4 $
3	4.2659435	$\tanh(\lambda_4)$
5	4.1934953	$\exp\left(\frac{1}{1 + \frac{1}{ \lambda_4 }}\right)$
7	2.741825	$0.22195499 \lambda_4 $
8	2.7418249	$\tanh(0.22568963) \lambda_4 $
9	2.4547632	$\frac{1}{1 + \frac{1}{ \lambda_4 } - 0.8714446}$
12	2.0753813	$\min(0.38399717 \lambda_4 , 7.041212)$
15	2.0627658	$\min(0.39465824 \min(\lambda_4 , \lambda_3), 7.0523863)$
16	1.9694929	$\min\left(\frac{1}{1 + \exp\left(\frac{1}{1 + \lambda_3 + \lambda_3}\right)} \lambda_4 , 6.8211412\right)$

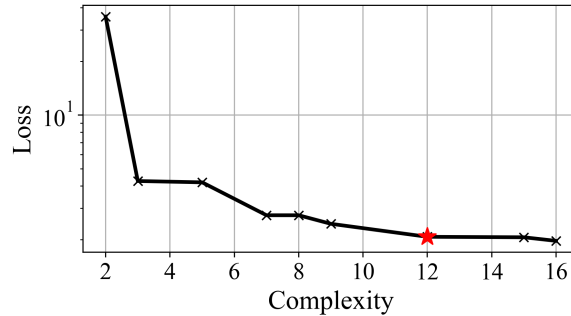


Figure 6. The loss-complexity plot of the final expressions

4. Test cases

In this section, the SST-CND3D model is tested in various 2D and 3D cases. In the 2D cases, the SST-CND3D model is expected to perform nearly identically to the SST-CND model, whereas in the 3D cases, the SST-CND3D model provides more accurate results than the SST-CND model.

4.1. 2D test cases

The SST-CND3D model is tested on the ZPG turbulent flat plate, the NASA hump case, and the NLR7301 multi-element airfoil [36]. The computational grid used for the ZPG turbulent flat plate is shown in Figure 7. It contains 133 faces along the wall and 97 cells in the wall-normal direction. The average Δy^+ of the first layer is approximately 0.2. The flow is incompressible, and OpenFOAM's SimpleFoam solver is used for this case. Figure 8 indicates that, in terms of the friction distribution along the plate and the velocity profile, the SST-CND3D model, the SST-CND model, and the SST model yield nearly identical outcomes. All three models produce skin friction consistent with the experimental data [37][38]. This result indicates that the SST-CND3D model retains the same accuracy as the baseline SST model in important wall-attached flows such as the ZPG turbulent flat plate.

The mesh used for the NASA hump case is shown in Figure 9. The flow is essentially incompressible, and OpenFOAM's SimpleFoam solver is used for this case. The Reynolds number based on the hump's chord length is approximately 9×10^5 . A total of 1156 cells are used in the streamwise direction, and 304 cells are used in the wall-normal direction. The average Δy^+ of the first layer is approximately 0.2. Figure 10(a) shows that the SST-CND3D model performs nearly identically to the SST-CND model, outperforming the SST model in predicting the reattachment point. The profiles of the correction term β are plotted in Figure 10(b). The correction term β is defined as $\beta = (\beta_{CND} + \beta_{3D})f_d + 1$ for the SST-CND3D model and $\beta = \beta_{CND}f_d + 1$ for the SST-CND model. The almost identical profiles of β indicate that β_{3D} is nearly zero in 2D flows. Accordingly, the new β_{3D} augmentation in the SST-CND3D model does not alter the already

established performance of the SST-CND model in 2D incompressible flows.

The grid for the NLR7301 multi-element airfoil is shown in Figure 11. The Reynolds number based on the chord length of the clean airfoil is $Re = 2.51 \times 10^6$, while the freestream Mach number is 0.185. The compressible solver CFL3D is used for this case. Figure 12 shows the $C_L - AOA$ curve computed by different models. The SST-CND3D and SST-CND models provide nearly identical C_L predictions. Both models outperform the baseline SST model in predicting the stall of the multi-element airfoil. Figure 13 shows the β distribution given by the SST-CND and SST-CND3D models. Both models activate the correction term in the mixing region above the flap, where the wake of the main wing and the jet formed by the slot are mixed. The nearly identical results of the SST-CND3D and SST-CND models in Figure 12 and Figure 13 demonstrate that the β_{3D} augmentation does not affect the SST-CND model's established performance in 2D compressible flows.

Accordingly, these test cases demonstrate that the SST-CND3D model, with the deliberately constructed β_{3D} correction term that vanishes in 2D scenarios, preserves the SST-CND model's high accuracy in important 2D wall-attached and complex separated flows. The sequential correction approach maintains the SST-CND model's performance in 2D cases.

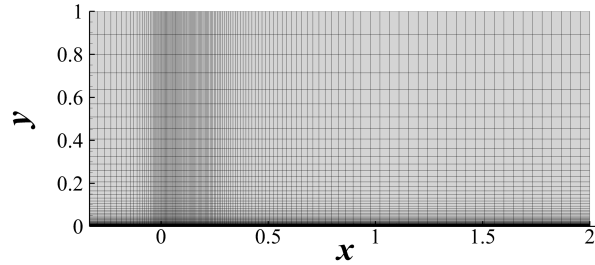


Figure 7. Computational grid of the ZPG turbulent flat plate case

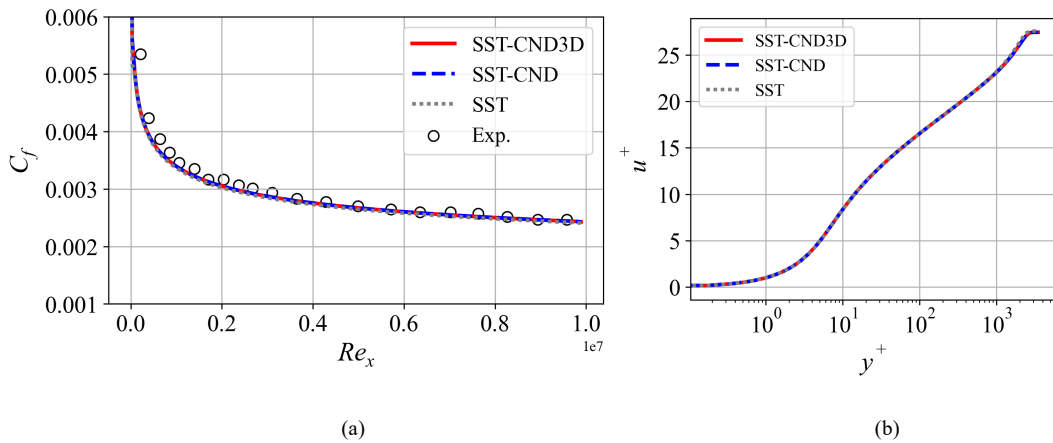


Figure 8. Results of the turbulent flat plate, (a) C_f distribution, (b) Velocity profile

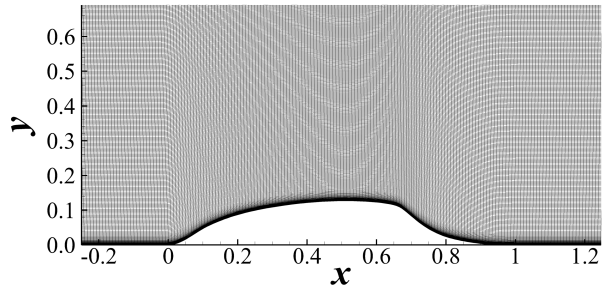


Figure 9. Computational grid of the NASA hump case

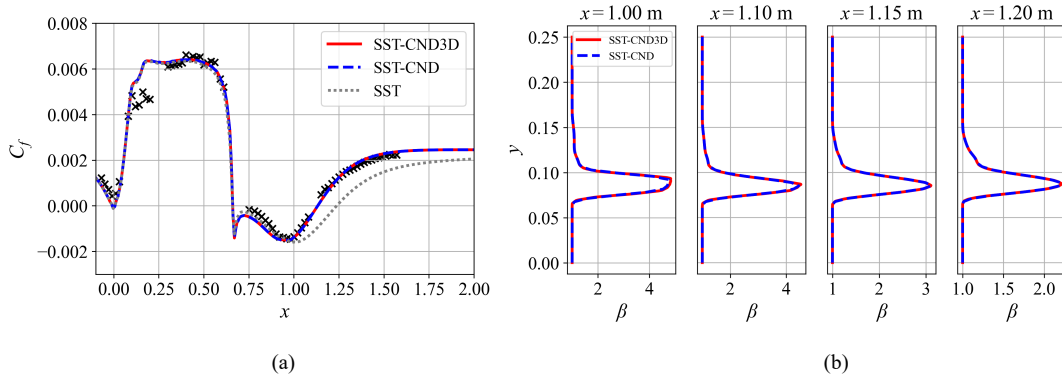


Figure 10. Results of the NASA hump, (a) C_f distribution, (b) β profiles

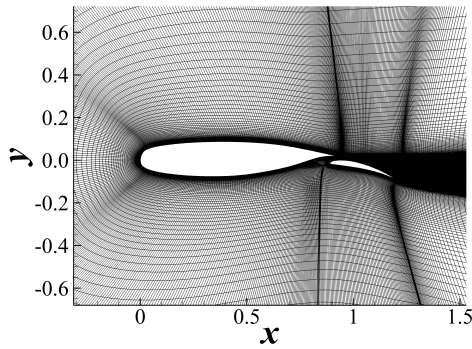


Figure 11. Computational grid of the NLR7301 multi-element airfoil

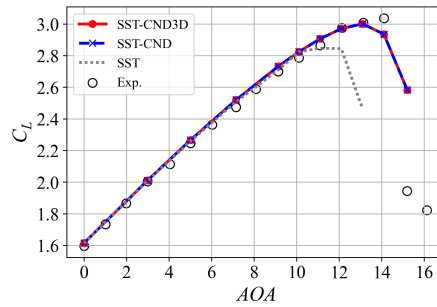


Figure 12. $C_L - AOA$ curve predicted by different models

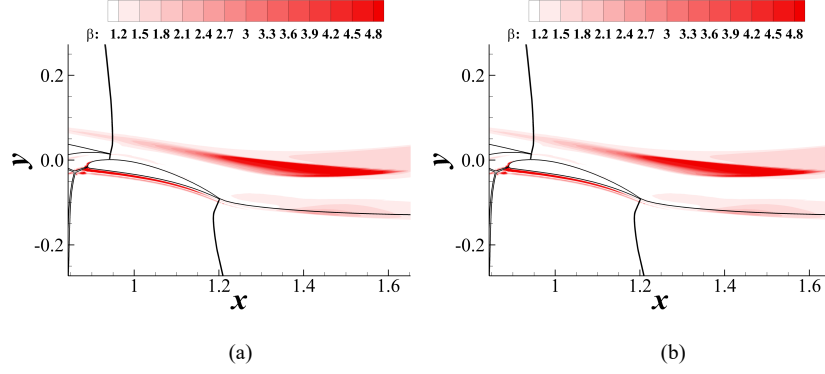


Figure 13. β contour given by (a) SST-CND model, (b) SST-CND3D model

4.2. Flow around a cube

The SST-CND3D model is applied to the training set of the β_{3D} correction term, corresponding to the cube case. The computational grid used is identical to that employed in the field inversion process. The contours of β obtained by the SST-CND model and the SST-CND3D model are illustrated in Figure 14 and Figure 15, respectively. Unlike the 2D cases, the SST-CND3D model produces a considerably larger β compared to the SST-CND model in the separated shear layer around the cube. A more distinct β is also observed in front of the cube. The reattachment point on the symmetry plane predicted by the SST-CND3D model moves forward compared to the prediction of the SST-CND model. The difference between Figure 14 and Figure 15 indicates that the β_{3D} term is activated in 3D scenarios. The velocity profiles and the C_p distribution predicted by the SST-CND3D model are closer to the experimental data than those predicted by the SST-CND model, as shown in Figure 16(a) and (b).

Accordingly, the results demonstrate that the SST-CND3D model achieves higher accuracy compared to the SST-CND model in the 3D training set of the β_{3D} augmentation term. The augmentation term β_{3D} generated by the sequential correction approach effectively improves the SST-CND model's performance in 3D scenarios.

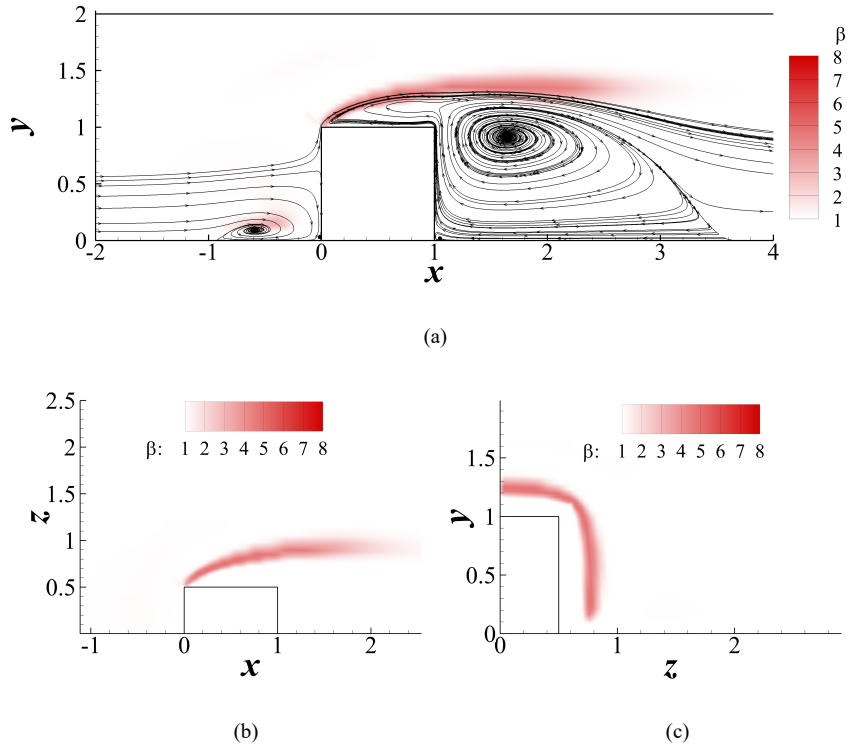


Figure 14. Contour of β obtained by the SST-CND model on the: (a) Symmetry plane ($z = 0$), (b) $y = 0.5 \text{ m}$ plane, (c) $x = 0.5 \text{ m}$ plane.

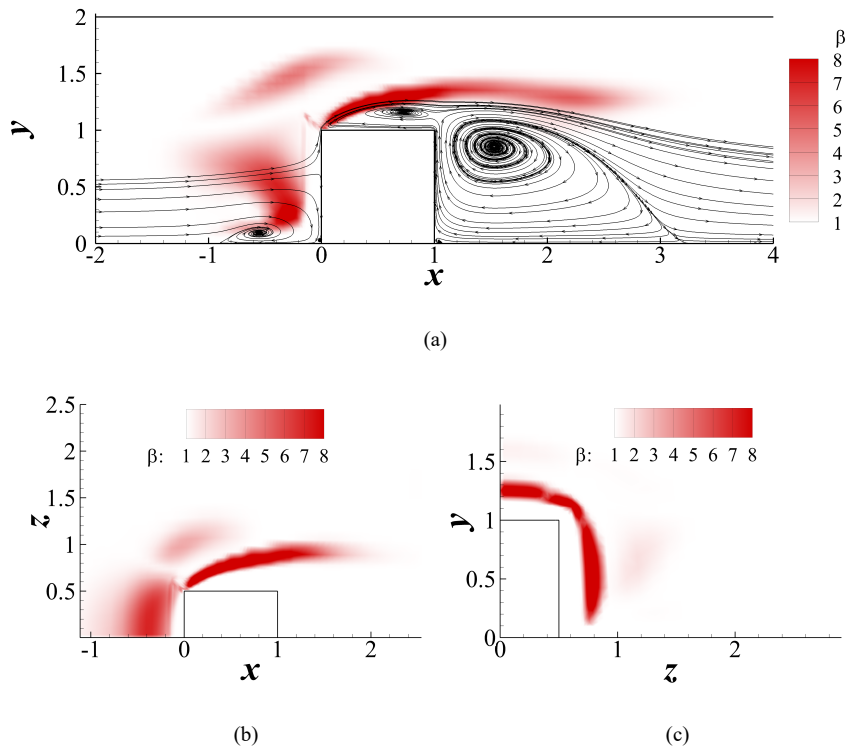


Figure 15. Contour of β obtained by the SST-CND3D model on the: (a) Symmetry plane ($z = 0$), (b) $y = 0.5 \text{ m}$ plane, (c) $x = 0.5 \text{ m}$ plane.

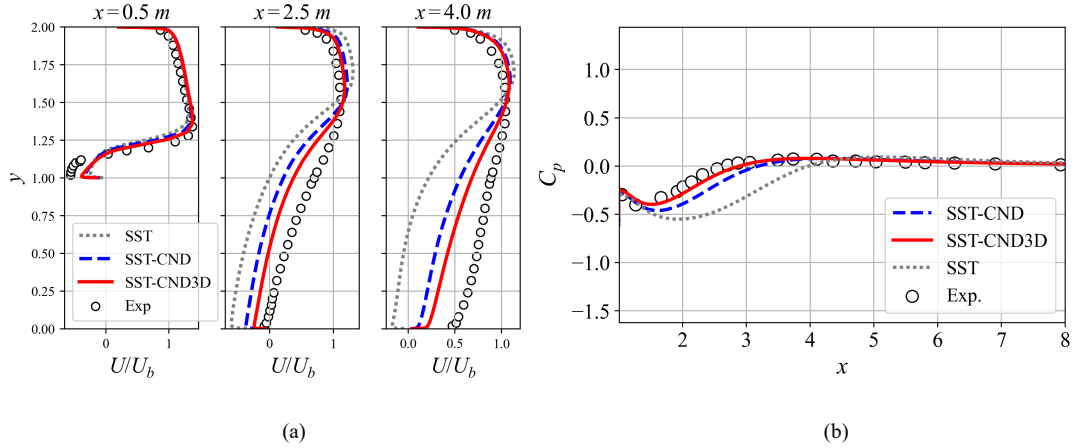


Figure 16. Results of different models, (a) Velocity profiles, (b) C_p distribution

4.3. Flow around a complex 3D high-lift configuration

In this section, the model is tested using the JAXA Standard Model (JSM) [39], which represents a complex 3D high-lift configuration. The geometry of the JSM is depicted in Figure 17. 3D structured grid is utilized for computation, as illustrated in Figure 18. The nacelles and pylons are included in the model, as well as the flap track and slat track fairings. A total of 96 million grid cells is used, and the average Δy^+ of the first layer is approximately 0.4. The freestream Mach number is 0.172, and the Reynolds number based on the mean aerodynamic chord is 1.93 million.

Initially, the force coefficients predicted by different models are compared. Figure 19(a) exhibits that the C_L at large AOA predicted by the SST-CND3D model is closer to the experimental data than the C_L predicted by the SST-CND model. Table 4 confirms that the SST-CND3D model provides more accurate predictions of $C_{L,max}$ and AOA_{stall} . The error of $C_{L,max}$ decreases by nearly 50% compared to the SST-CND model. The polar curve in Figure 19(b) also indicates a better prediction of C_D at large C_L . In addition, the SST-CND3D model provides a more accurate C_m compared to the SST-CND model at high C_L , as shown in Figure 19(c). This finding indicates that the SST-CND3D model achieves a more realistic force distribution along the JSM body.

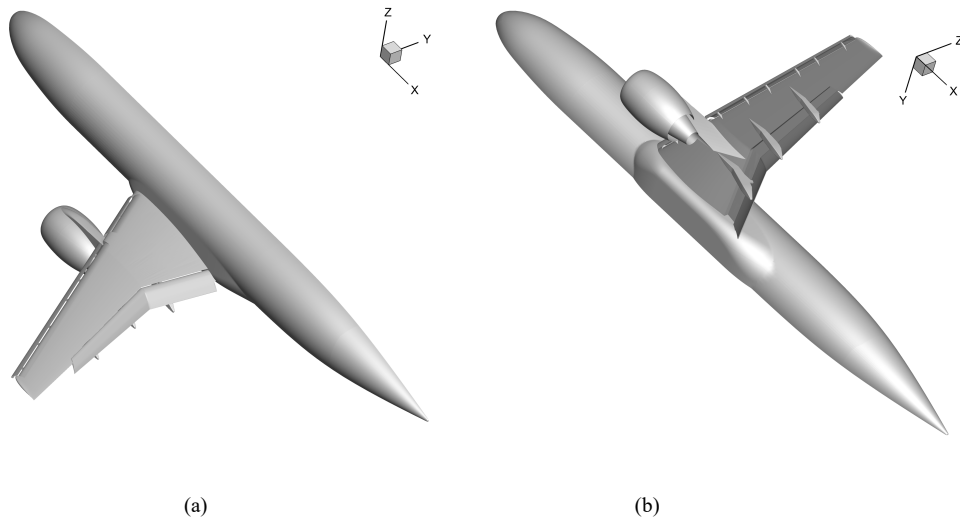


Figure 17. Geometry of the JAXA standard model (JSM), (a) Upper view, (b) Lower view

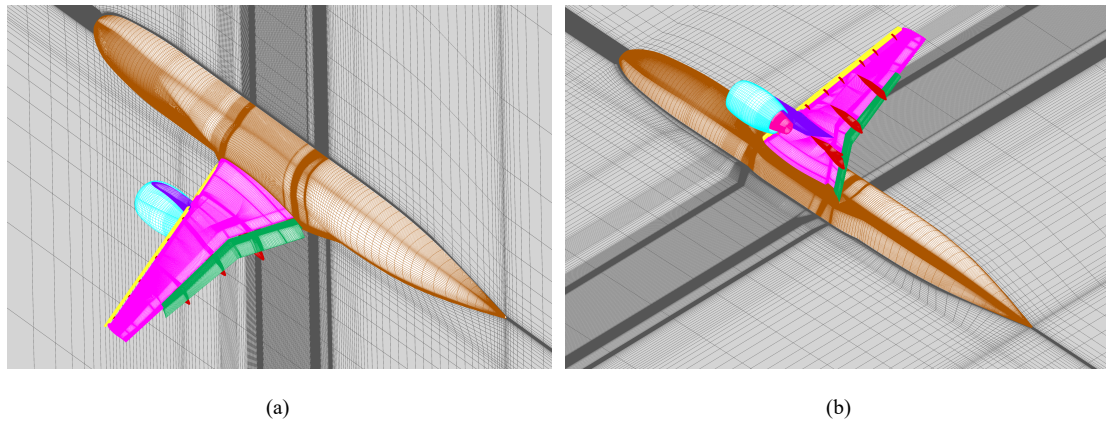
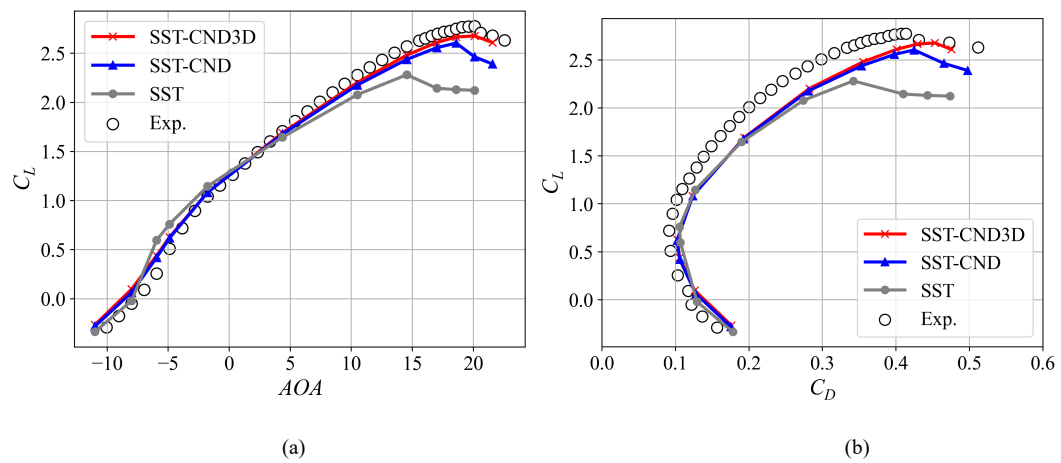
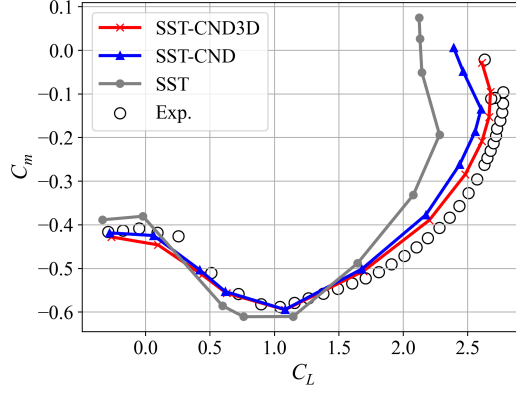


Figure 18. 3D structured grid used for computation, the grid is coarsened for clarity, (a) Upper view, (b) Lower view





(c)

Figure 19. Force coefficients predicted by different models, (a) $C_L - AOA$ curve, (b) $C_L - C_D$ curve, (c) $C_m - C_L$ curve

Table 4. Prediction value and error of the maximum lift coefficient and stall angle of attack

	SST	SST-CND	SST-CND3D	Exp.
$AOA_{stall}/\text{difference}$	14.54°/5.55°	18.59°/1.5°	20.09°/0°	20.09°/-
$C_{L,max}/\text{error}$	2.282/17.8%	2.604/6.2%	2.677/3.5%	2.775/-

Figure 20 presents the surface streamline plot of the JSM at $AOA = 18.6^\circ$. It can be observed that the SST model predicts a large separation zone in the middle of the wing. The SST-CND and SST-CND3D models both predict attached flow, consistent with the oil flow image in Figure 20(d). The surface streamline plots of the SST-CND and SST-CND3D models appear similar; however, the SST-CND3D model predicts a relatively smaller separation in the outboard region of the wing and at the wing root, where the 3D effect is more pronounced. Figure 21 shows the pressure coefficient distribution along six different sections of the wing at $AOA = 18.6^\circ$. The SST model underpredicts the suction peak of the wing, and a flat C_p distribution caused by flow separation is visible at section E–E. Both the SST-CND and SST-CND3D models yield results that agree better with the experimental data. However, at section H–H, all models underpredict the suction peak, with the SST-CND3D model performing slightly better. Figure 22 displays the C_p distribution at $AOA = 20.6^\circ$, corresponding to the post-stall condition. At section E–E (the middle of the wing), the SST and SST-CND models both produce a flat C_p distribution resulting from flow separation, while the SST-CND3D model performs significantly better and matches the experimental data. At the outboard sections of the wing (G–G and H–H), the SST-CND3D model also provides a stronger suction that corresponds more closely with the experiment. The contour of β at $y = -1.0\text{ m}$ and the spatial streamlines (projection) are shown in Figure 23. The SST-CND3D model exhibits a larger

correction term β extending from the wake of the main wing, effectively suppressing the size of the separation bubble.

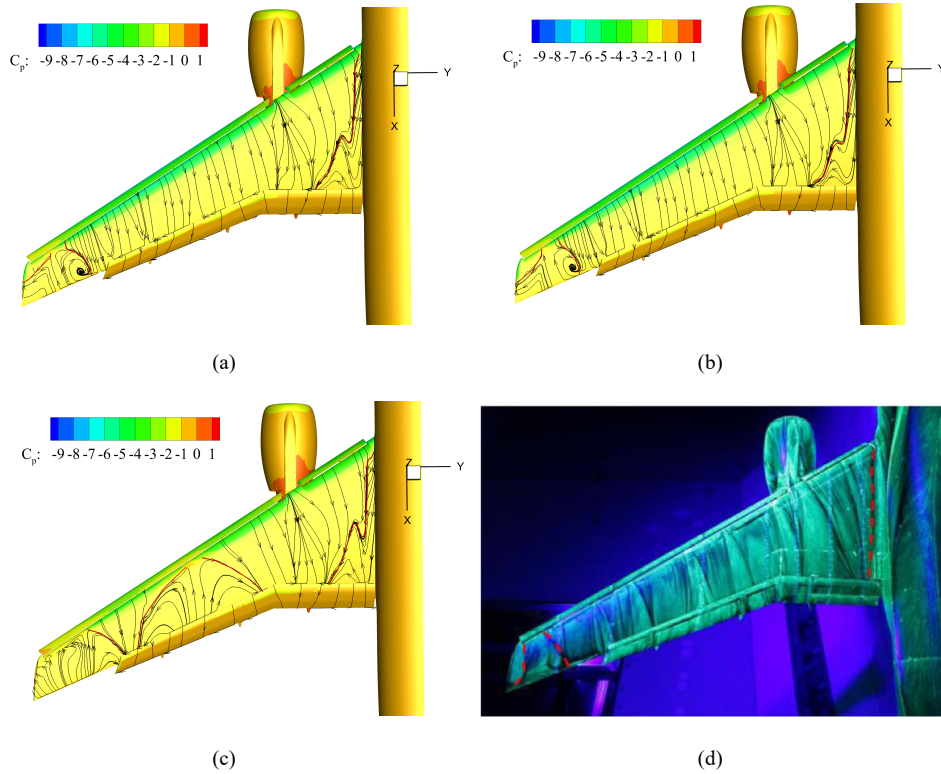
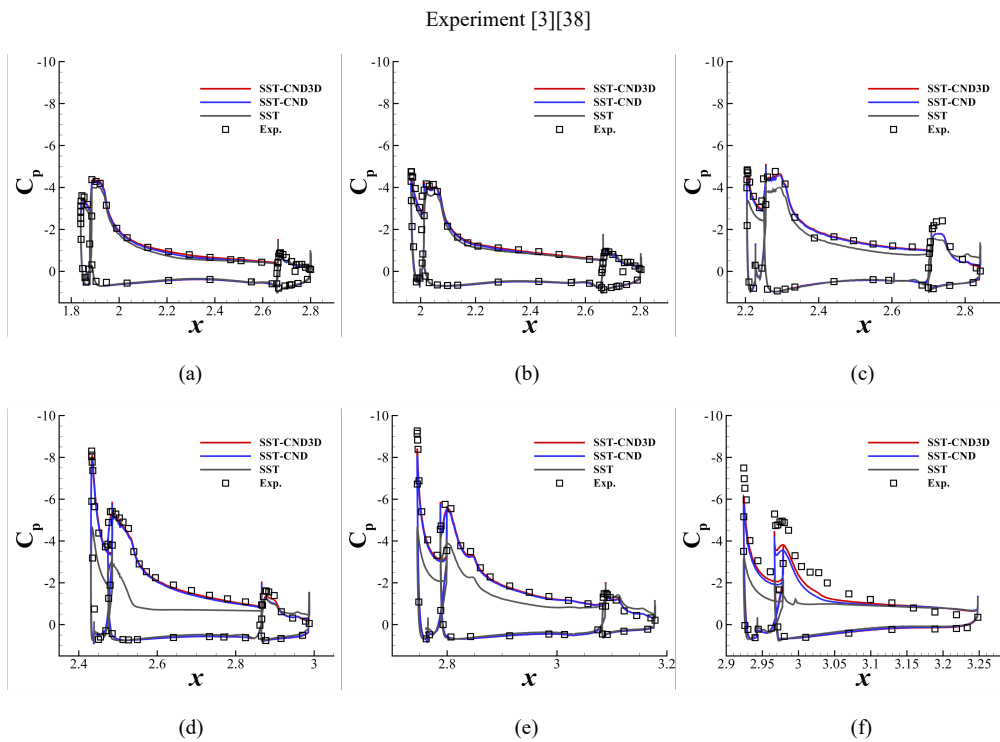


Figure 20. Surface streamline plot at $AOA = 18.6^\circ$ given by (a) SST-CND model, (b) SST-CND3D model, (c) SST model, (d)



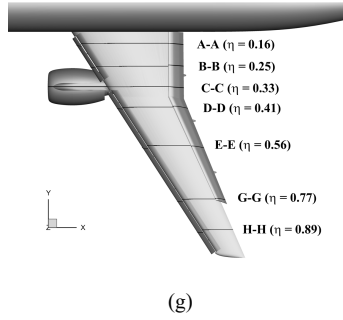


Figure 21. C_p distribution along different sections in the spanwise direction at $AOA = 18.6^\circ$, (a) A-A section, (b) B-B section,

(c) D-D section, (d) E-E section, (e) G-G section, (f) H-H section, (g) Location of different sections

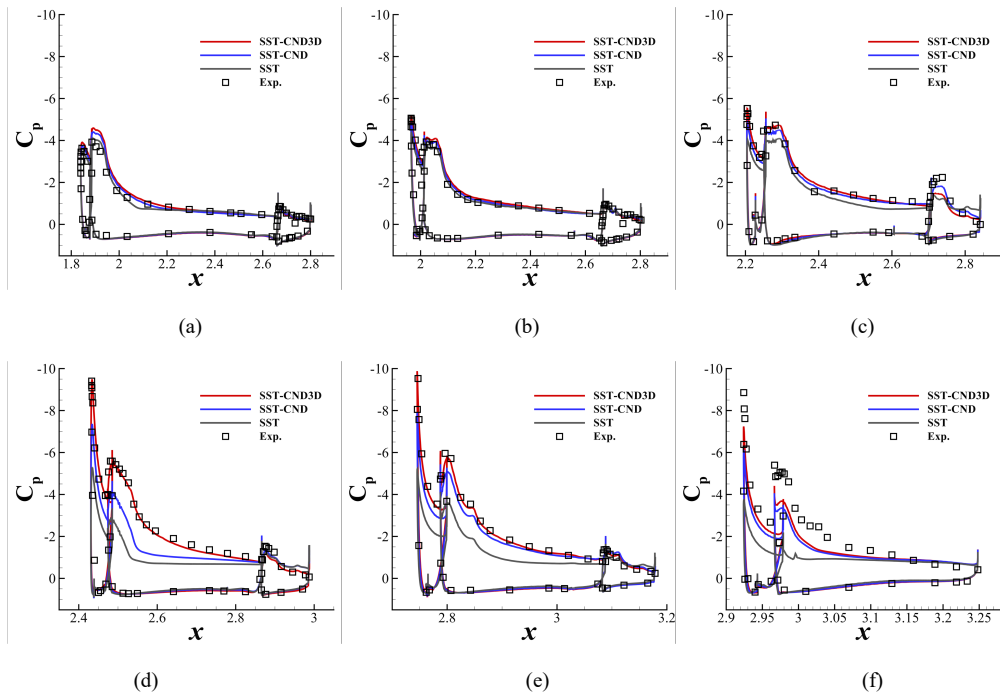


Figure 22. C_p distribution along different sections in the spanwise direction at $AOA = 20.6^\circ$, (a) A-A section, (b) B-B section,

(c) D-D section, (d) E-E section, (e) G-G section, (f) H-H section

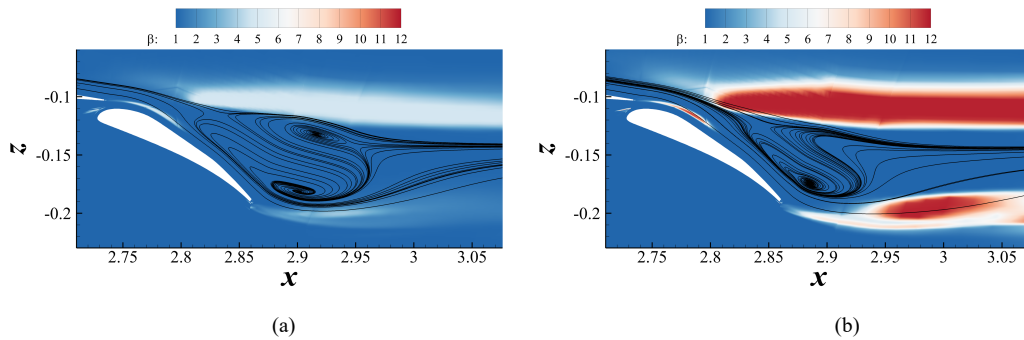


Figure 23. β distribution and the streamline plot (based on u_x and u_z) given by different models at $y = -1.0$ m, $AOA = 18.6^\circ$, (a) SST-CND model, (b) SST-CND3D model.

Accordingly, the SST-CND3D model outperforms the SST-CND model in the JSM case. The

results confirm the effectiveness of the β_{3D} correction term constructed through sequential correction and highlights the potential of the SST-CND3D model for application in real-world complex engineering problems.

5. Conclusions

This study successfully enhances the SST-CND model's performance in 3D complex flows without retraining the model from scratch or compromising its established accuracy in 2D separated flows employing a sequential correction approach. This approach non-intrusively augments the existing SST-CND model by constructing a new 3D-specific correction term, β_{3D} , on top of the original formulation. The input features for β_{3D} are designed to explicitly vanish in 2D scenarios, ensuring that the correction term primarily accounts for the 3D effects. The explicit algebraic form of β_{3D} is determined through a combination of field inversion using 3D cube flow data and symbolic regression. The final expression is selected to ensure that it vanishes in 2D flows. The resultant SST-CND3D model demonstrates identical accuracy to the SST-CND model across all 2D validation cases (hump, flat plate, and multi-element airfoil). The SST-CND3D model in 3D flows achieves superior accuracy compared to the SST-CND model, effectively addressing the underprediction issues of C_L and AOA_{stall} observed in the complex JSM configuration.

This study validates the sequential correction approach as a robust and efficient method for enhancing existing data-driven turbulence models. It enables the incorporation of higher-dimensional data to improve generalization while avoiding the risks and computational costs associated with retraining the entire model. The developed model demonstrates strong potential for application in real-world complex engineering problems.

Appendix

A.1 Proof of $\lambda_3 = 0$ and $\lambda_4 = 0$ in 2D incompressible flows

For λ_3 , it can be written as follows:

$$\lambda_3 = \text{tr}(\widehat{\mathbf{S}}^3) = \left(\frac{k}{\varepsilon}\right)^3 \text{tr}(\mathbf{S}^3) \quad (25)$$

It must prove that $\text{tr}(\mathbf{S}^3)$ equals to zero in 2D incompressible flows. Since the flow is 2D, it can be assumed that $u_3 = 0$ and $\frac{\partial(\cdot)}{\partial x_3} = 0$, then the (corresponding matrix of) strain rate tensor is:

$$\mathbf{S} = \begin{pmatrix} \frac{\partial u_1}{\partial x_1} & \frac{1}{2} \left(\frac{\partial u_1}{\partial x_2} + \frac{\partial u_2}{\partial x_1} \right) & 0 \\ \frac{1}{2} \left(\frac{\partial u_1}{\partial x_2} + \frac{\partial u_2}{\partial x_1} \right) & \frac{\partial u_2}{\partial x_2} & 0 \\ 0 & 0 & 0 \end{pmatrix} \quad (26)$$

Performing matrix multiplication indicates that:

$$\mathbf{S}^2 = \begin{pmatrix} \left(\frac{\partial u_1}{\partial x_1} \right)^2 + \left[\frac{1}{2} \left(\frac{\partial u_1}{\partial x_2} + \frac{\partial u_2}{\partial x_1} \right) \right]^2 & \frac{1}{2} \left(\frac{\partial u_1}{\partial x_2} + \frac{\partial u_2}{\partial x_1} \right) \left(\frac{\partial u_1}{\partial x_1} + \frac{\partial u_2}{\partial x_2} \right) & 0 \\ \frac{1}{2} \left(\frac{\partial u_1}{\partial x_2} + \frac{\partial u_2}{\partial x_1} \right) \left(\frac{\partial u_1}{\partial x_1} + \frac{\partial u_2}{\partial x_2} \right) & \left(\frac{\partial u_2}{\partial x_2} \right)^2 + \left[\frac{1}{2} \left(\frac{\partial u_1}{\partial x_2} + \frac{\partial u_2}{\partial x_1} \right) \right]^2 & 0 \\ 0 & 0 & 0 \end{pmatrix} \quad (27)$$

For the flow is incompressible, there is:

$$\nabla \cdot \mathbf{u} = \frac{\partial u_1}{\partial x_1} + \frac{\partial u_2}{\partial x_2} + \frac{\partial u_3}{\partial x_3} = \frac{\partial u_1}{\partial x_1} + \frac{\partial u_2}{\partial x_2} = 0 \quad (28)$$

Inserting Eq. (28) into Eq. (27) shows that:

$$\begin{aligned} \mathbf{S}^2 &= \begin{pmatrix} \left(\frac{\partial u_1}{\partial x_1} \right)^2 + \left[\frac{1}{2} \left(\frac{\partial u_1}{\partial x_2} + \frac{\partial u_2}{\partial x_1} \right) \right]^2 & 0 & 0 \\ 0 & \left(\frac{\partial u_1}{\partial x_1} \right)^2 + \left[\frac{1}{2} \left(\frac{\partial u_1}{\partial x_2} + \frac{\partial u_2}{\partial x_1} \right) \right]^2 & 0 \\ 0 & 0 & 0 \end{pmatrix} \\ &= \left(\left(\frac{\partial u_1}{\partial x_1} \right)^2 + \left[\frac{1}{2} \left(\frac{\partial u_1}{\partial x_2} + \frac{\partial u_2}{\partial x_1} \right) \right]^2 \right) \begin{pmatrix} 1 & 0 & 0 \\ 0 & 1 & 0 \\ 0 & 0 & 0 \end{pmatrix} \end{aligned} \quad (29)$$

Therefore, \mathbf{S}^3 can be written as follows:

$$\mathbf{S}^3 = \left(\left(\frac{\partial u_1}{\partial x_1} \right)^2 + \left[\frac{1}{2} \left(\frac{\partial u_1}{\partial x_2} + \frac{\partial u_2}{\partial x_1} \right) \right]^2 \right) \begin{pmatrix} \frac{\partial u_1}{\partial x_1} & \frac{1}{2} \left(\frac{\partial u_1}{\partial x_2} + \frac{\partial u_2}{\partial x_1} \right) & 0 \\ \frac{1}{2} \left(\frac{\partial u_1}{\partial x_2} + \frac{\partial u_2}{\partial x_1} \right) & \frac{\partial u_2}{\partial x_2} & 0 \\ 0 & 0 & 0 \end{pmatrix} \quad (30)$$

Taking the trace of \mathbf{S}^3 and considering Eq. (28), yields:

$$\text{tr}(\mathbf{S}^3) = \left(\left(\frac{\partial u_1}{\partial x_1} \right)^2 + \left[\frac{1}{2} \left(\frac{\partial u_1}{\partial x_2} + \frac{\partial u_2}{\partial x_1} \right) \right]^2 \right) \left(\frac{\partial u_1}{\partial x_1} + \frac{\partial u_2}{\partial x_2} \right) = 0 \quad (31)$$

Therefore, $\lambda_3 = \left(\frac{k}{\varepsilon} \right)^3 \text{tr}(\mathbf{S}^3) = 0$.

For λ_4 , it can be described as follows:

$$\lambda_4 = \text{tr}(\hat{\boldsymbol{\Omega}}^2 \hat{\mathbf{S}}) = \left(\frac{k}{\varepsilon} \right)^3 \text{tr}(\boldsymbol{\Omega}^2 \mathbf{S}) \quad (32)$$

The rotation rate tensor is:

$$\mathbf{\Omega} = \begin{pmatrix} 0 & \frac{1}{2} \left(\frac{\partial u_1}{\partial x_2} - \frac{\partial u_2}{\partial x_1} \right) & 0 \\ -\frac{1}{2} \left(\frac{\partial u_1}{\partial x_2} - \frac{\partial u_2}{\partial x_1} \right) & 0 & 0 \\ 0 & 0 & 0 \end{pmatrix} \quad (33)$$

Then, $\mathbf{\Omega}^2$ is:

$$\begin{aligned} \mathbf{\Omega}^2 &= \begin{pmatrix} -\left[\frac{1}{2} \left(\frac{\partial u_1}{\partial x_2} - \frac{\partial u_2}{\partial x_1} \right) \right]^2 & 0 & 0 \\ 0 & -\left[\frac{1}{2} \left(\frac{\partial u_1}{\partial x_2} - \frac{\partial u_2}{\partial x_1} \right) \right]^2 & 0 \\ 0 & 0 & 0 \end{pmatrix} \\ &= -\left[\frac{1}{2} \left(\frac{\partial u_1}{\partial x_2} - \frac{\partial u_2}{\partial x_1} \right) \right]^2 \begin{pmatrix} 1 & 0 & 0 \\ 0 & 1 & 0 \\ 0 & 0 & 0 \end{pmatrix} \end{aligned} \quad (34)$$

That is to say, $\mathbf{\Omega}^2 \mathbf{S}$ can be written as follows:

$$\mathbf{\Omega}^2 \mathbf{S} = -\left[\frac{1}{2} \left(\frac{\partial u_1}{\partial x_2} - \frac{\partial u_2}{\partial x_1} \right) \right]^2 \begin{pmatrix} \frac{\partial u_1}{\partial x_1} & \frac{1}{2} \left(\frac{\partial u_1}{\partial x_2} + \frac{\partial u_2}{\partial x_1} \right) & 0 \\ \frac{1}{2} \left(\frac{\partial u_1}{\partial x_2} + \frac{\partial u_2}{\partial x_1} \right) & \frac{\partial u_2}{\partial x_2} & 0 \\ 0 & 0 & 0 \end{pmatrix} \quad (35)$$

Taking the trace of Eq. (35) and inserting Eq. (28), produces:

$$\text{tr}(\mathbf{\Omega}^2 \mathbf{S}) = -\left[\frac{1}{2} \left(\frac{\partial u_1}{\partial x_2} - \frac{\partial u_2}{\partial x_1} \right) \right]^2 \left(\frac{\partial u_1}{\partial x_1} + \frac{\partial u_2}{\partial x_2} \right) = 0 \quad (36)$$

Therefore, $\lambda_4 = \left(\frac{k}{\varepsilon} \right)^3 \text{tr}(\mathbf{\Omega}^2 \mathbf{S}) = 0$.

Acknowledgement

This work was supported by the National Natural Science Foundation of China (grant numbers 12372288, U23A2069, and 12388101), the National Key Research and Development Program of China (2024YFB4205601), and other national research projects. AI is used to polish the writing of the paper.

Reference

- [1] Rumsey, C. L. Exploring a method for improving turbulent separated-flow predictions with k-omega models. (2009).

- [2] Aqilah, F., et al. CFD analysis around Ahmed body using a laminar kinetic energy based transition and turbulence model. Proceedings of the Topical Problems of Fluid Mechanics, pp. 1–6 (2019).
- [3] Li, H., Zhang, Y., and Chen, H. "Aerodynamic prediction of iced airfoils based on modified three-equation turbulence model." *AIAA Journal* 58(9), 3863–3876 (2020).
- [4] Zhang, S., et al. "Aerodynamic prediction of high-lift configuration using $k-v^2-\omega$ turbulence model." *AIAA Journal* 60(5), 2916–2929 (2022).
- [5] Zhang, S., Li, H., and Zhang, Y. "Aerodynamic prediction of the high-lift common research model with modified turbulence model." *AIAA Journal* 62(7), 2723–2744 (2024).
- [6] Duraisamy, K., Spalart, P. R., and Rumsey, C. L. Status, emerging ideas and future directions of turbulence modeling research in aeronautics. NASA/TM-2017-219682 (2017).
- [7] Duraisamy, K., Iaccarino, G., and Xiao, H. "Turbulence modeling in the age of data." *Annual Review of Fluid Mechanics* 51(1), 357–377 (2019).
- [8] Ling, J., Kurzawski, A., and Templeton, J. "Reynolds averaged turbulence modelling using deep neural networks with embedded invariance." *Journal of Fluid Mechanics* 807, 155–166 (2016).
- [9] Yin, Y., et al. "Feature selection and processing of turbulence modeling based on an artificial neural network." *Physics of Fluids* 32(10), 105107 (2020).
- [10] Tang, H., et al. "Discovering explicit Reynolds-averaged turbulence closures for turbulent separated flows through deep learning-based symbolic regression with non-linear corrections." *Physics of Fluids* 35(2), 025121 (2023).
- [11] Zhao, Y., et al. "RANS turbulence model development using CFD-driven machine learning." *Journal of Computational Physics* 411, 109413 (2020).
- [12] Singh, A. P., Medida, S., and Duraisamy, K. "Machine-learning-augmented predictive modeling of turbulent separated flows over airfoils." *AIAA Journal* 55(7), 2215–2227 (2017).
- [13] Holland, J. R., Baeder, J. D., and Duraisamy, K. Field inversion and machine learning with embedded neural networks: Physics-consistent neural network training. AIAA Aviation Forum, AIAA Paper 2019-3200 (2019).
- [14] Wu, C., and Zhang, Y. "Enhancing the shear-stress-transport turbulence model with symbolic regression: A generalizable and interpretable data-driven approach." *Physical Review Fluids* 8(8), 084604 (2023).
- [15] Zhang, S., Wu, C., and Zhang, Y. "Three-dimensional high-lift configuration simulation using data-driven turbulence model." *Physics of Fluids* 37(7), 075104 (2025).
- [16] Wu, C., Zhang, S., and Zhang, Y. "Development of a generalizable data-driven turbulence model: Conditioned field inversion and symbolic regression." *AIAA Journal* 63(2), 687–706 (2025).
- [17] Ho, J., and West, A. Field inversion and machine learning for turbulence modelling applied to three-dimensional separated flows. AIAA Aviation Forum, AIAA Paper 2021-2903 (2021).

- [18] Yan, C., Zhang, Y., and Chen, H. "Data augmented turbulence modeling for three-dimensional separation flows." *Physics of Fluids* 34(7), 075103 (2022).
- [19] Bell, J., et al. Surface and flow field measurements on the Faith Hill model. 50th AIAA Aerospace Sciences Meeting Including the New Horizons Forum and Aerospace Exposition, AIAA Paper 2012-0704 (2012).
- [20] Sun, X., et al. "Development and deployment of data-driven turbulence model for three-dimensional complex configurations." *Machine Learning: Science and Technology* 5(3), 035085 (2024).
- [21] Steiner, J., Dwight, R., and Viré, A. "Data-driven turbulence modeling for wind turbine wakes under neutral conditions." *Journal of Physics: Conference Series* 1618(6), 062026 (2020).
- [22] Avdis, A., Lardeau, S., and Leschziner, M. "Large eddy simulation of separated flow over a two-dimensional hump with and without control by means of a synthetic slot-jet." *Flow, Turbulence and Combustion* 83(3), 343–370 (2009).
- [23] Bentaleb, Y., Lardeau, S., and Leschziner, M. A. "Large-eddy simulation of turbulent boundary layer separation from a rounded step." *Journal of Turbulence* 13, N4 (2012).
- [24] Menter, F. R. "Two-equation eddy-viscosity turbulence models for engineering applications." *AIAA Journal* 32(8), 1598–1605 (1994).
- [25] Gill, P. E., Murray, W., and Saunders, M. A. "SNOPT: An SQP algorithm for large-scale constrained optimization." *SIAM Review* 47(1), 99–131 (2005).
- [26] Jameson, A., and Kim, S. "Reduction of the adjoint gradient formula for aerodynamic shape optimization problems." *AIAA Journal* 41(11), 2114–2129 (2003).
- [27] He, P., et al. "An aerodynamic design optimization framework using a discrete adjoint approach with OpenFOAM." *Computers & Fluids* 168, 285–303 (2018).
- [28] He, P., et al. "Dafoam: An open-source adjoint framework for multidisciplinary design optimization with OpenFOAM." *AIAA Journal* 58(3), 1304–1319 (2020).
- [29] Sagebaum, M., Albring, T., and Gauger, N. R. "High-performance derivative computations using CoDiPack." *ACM Transactions on Mathematical Software (TOMS)* 45(4), 1–26 (2019).
- [30] Pope, S. B. "A more general effective-viscosity hypothesis." *Journal of Fluid Mechanics* 72(2), 331–340 (1975).
- [31] Wilcox, D. C. "Formulation of the $k-\omega$ turbulence model revisited." *AIAA Journal* 46(11), 2823–2838 (2008).
- [32] Cranmer, M. Interpretable machine learning for science with PySR and SymbolicRegression.jl. arXiv preprint arXiv:2305.01582 (2023).
- [33] Martinuzzi, R., and Tropea, C. The flow around surface-mounted, prismatic obstacles placed in a fully developed channel flow (data bank contribution). pp. 85–92 (1993)
- [34] Jasak, H. "OpenFOAM: Open source CFD in research and industry." *International Journal of Naval Architecture and Ocean Engineering* 1(2), 89–94 (2009).

- [35] Rumsey, C. L. CFL3D Version 6 home page. NASA (1980).
<https://nasa.github.io/CFL3D/> [Retrieved 7 Oct. 2025] [Website].
- [36] Arlinger, B. G., and Larsson, T. NLR 7301 two element airfoil at high lift. Notes on Numerical Fluid Mechanics 58, 375–396 (1997).
- [37] Wiegardt, K., and Tillmann, W. On the turbulent friction layer for rising pressure. NACA-TM-1314 (1951).
- [38] OpenCFD Ltd. Turbulent flat plate. (2018).
<https://www.openfoam.com/documentation/guides/latest/doc/verification-validation-turbulent-flat-plate-zpg.html>
- [39] Rumsey, C. L., Slotnick, J. P., and Sclafani, A. J. Overview and summary of the third AIAA high lift prediction workshop. AIAA Aerospace Sciences Meeting (2018).